

On the Expansion, Age, and Origin of the Puzzling Shell/Pulsar Wind Nebula G310.6–1.6

STEPHEN P. REYNOLDS¹ AND KAZIMIERZ J. BORKOWSKI¹

¹*Department of Physics, North Carolina State University, Raleigh, NC 27695-8202, USA*

ABSTRACT

We present a 142-ks *Chandra* observation of the enigmatic combination supernova remnant G310.6–1.6 consisting of a bright pulsar-wind nebula driven by an energetic pulsar, surrounded by a highly circular, very faint shell with a featureless, probably synchrotron, spectrum. Comparison with an observation 6 years earlier shows no measurable expansion of the shell, though some features in the pulsar-wind nebula have moved. We find an expansion age of at least 2500 yr, implying a current shock velocity less than about 1000 km s⁻¹. We place severe upper limits on thermal emission from the shell; if the shell locates the blast wave, a Sedov interpretation would require the remnant to be very young, about 1000 yr, and to have resulted from a dramatically sub-energetic supernova, ejecting $\ll 0.02M_{\odot}$ with energy $E \lesssim 3 \times 10^{47}$ erg. Even a merger-induced collapse of a white dwarf to a neutron star, with a low-energy explosion, is unlikely to produce such an event. Other explanations seem equally unlikely.

Keywords: ISM: individual objects (G310.6–1.6) — ISM: supernova remnants — ISM: pulsar-wind nebulae — X-rays: ISM

1. INTRODUCTION

Pulsar-wind nebulae (PWNe) showcase the energy emitted by fast pulsars in some combination of Poynting flux and relativistic particles. Young PWNe, still inside their natal supernova remnants (SNRs), also exhibit the interaction of that relativistic material with the innermost ejecta from the supernova, thus connecting a range of important astrophysical phenomena: the pulsars themselves, the initially cold relativistic wind carrying a “striped” magnetic field, the relativistic termination shock thermalizing the relativistic-particle population somehow, the complex post-shock flow involving tori and disks, the outer boundary which might mark a “piston” driving a shock into the inner ejecta, and the entire shell SNR that the PWN inhabits.

The combination of a full-fledged PWN with observed pulsar surrounded by a normal-appearing shell SNR is surprisingly rare. Discovering and characterizing a new such system marks important progress in developing a sample from which common properties can be distinguished from individual differences. Such a system may be the remarkable combination object discovered by INTEGRAL as IGR J14003-6326, and associated with a recently discovered SNR/PWN as G310.6–1.6 (Renaud et al. 2010, hereafter R10). This object has features that make it unique among all SNRs in the Galaxy. Here we report new *Chandra* observations of G310.6–1.6.

2. G310.6–1.6

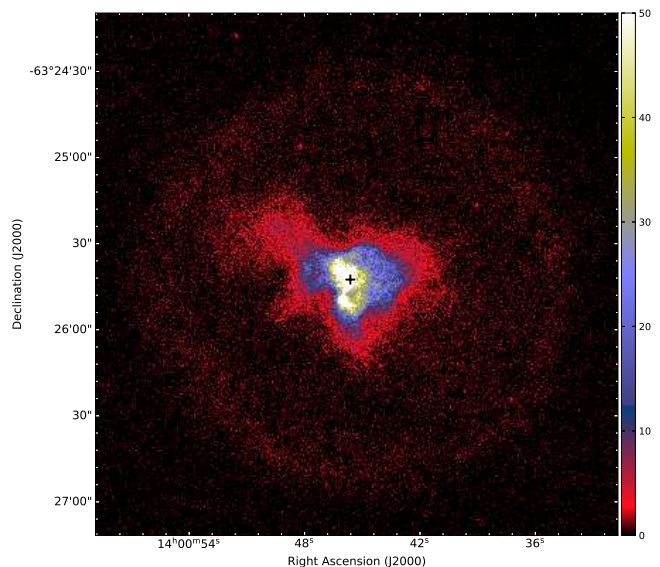


Figure 1. 142-ks *Chandra* image of G310.6–1.6 in 2016 in the 1–8 keV energy range (on linear scaling to emphasize its shell and the faint structure at the periphery of the PWN). The small (70'' in radius) shell is quite spherical but faint, with few (up to at most 3) counts per ACIS pixel detected. Significant spatial variations within the shell are apparent, although there are no obvious very sharp filaments as often found in other young SNRs. The central cross indicates the position of the pulsar.

The source IGR 14003-6326 was discovered in a deep INTEGRAL survey of the Circinus region (Keek et al. 2006) and identified as a small ($\theta \lesssim 1'$), highly absorbed ($N_H \sim$

$3 \times 10^{22} \text{ cm}^{-2}$) PWN in a 5.1 ks *Chandra* observation (Tomsick et al. 2009). R10 used *RXTE* observations to discover pulsations with a period of 31.18 ms and a \dot{P} implying a rotational energy-loss rate $\dot{E} = 5.1 \times 10^{37} \text{ erg s}^{-1}$, making it one of the most energetic pulsars known. They obtained spectra for the pulsar itself and the central PWN, and also reported a very faint almost circular shell surrounding the PWN, based on the short *Chandra* exposure. They christened this previously unknown shell SNR G310.6–1.6, a designation we shall use for the entire SNR/PWN system. See Figure 1. The PWN had a hard power-law spectrum, $\Gamma \sim 1.8$, and the shell, while faint, was well described by a softer power-law with $\Gamma \sim 2.6$. The distance was uncertain; the dispersion-measure distance of $10 \pm 3 \text{ kpc}$ would have placed G310.6–1.6 at a z -distance of 280 pc above the Galactic plane, rather high for a Pop I type object. However, R10 argued that the object might lie in the Crux-Scutum spiral arm closer to 7 kpc, and used that value in their analysis. (We shall adopt the 7 kpc distance, and quote results in terms of $d_7 \equiv d/7 \text{ kpc}$.) The shell has a very small angular diameter ($\sim 2.5'$), making it one of the smallest angular-size SNRs in the Galaxy, not much larger than the youngest Galactic remnant G1.9+0.3. While the PWN is bright, G310.6–1.6 has not been reported in either GeV or TeV gamma rays.

R10 interpreted the shell as the outer blast wave of a normal shell SNR, making this object an interesting new member of the composite class. The shell has a diameter of $5.1d_7 \text{ pc}$, and if produced by a 10^{51} -erg supernova ejecting $10M_{\odot}$, has an initial expansion velocity of 3200 km s^{-1} and an undecelerated (free expansion) age of only $780d_7 \text{ yr}$. However, from the size of the PWN relative to the shell and other arguments, R10 concluded that G310.6–1.6 represents the remnant of a very sub-energetic ($E \sim 5 \times 10^{49} \text{ erg}$) supernova that ejected about $3 M_{\odot}$ into a low-density medium ($n_0 \sim 0.01 \text{ cm}^{-3}$). This would imply an initial expansion velocity of only 1300 km s^{-1} , and a free-expansion age of 1900 yr (less with deceleration). Since the spin-down age $P/2\dot{P} = 12.7 \text{ kyr}$, this interpretation would require the pulsar to have been born at nearly its current period.

However, this interpretation – in fact, any interpretation – has significant problems accounting for all the properties of this peculiar object. A 51 ks *Chandra* observation was performed in 2010 (M. Renaud, PI) but has never been published, though it was analyzed as part of a bachelor’s thesis project at U. Tours (Berthiere 2012, B12). R10 and B12 show that the shell spectrum is dominantly nonthermal, with no hint of thermal emission. If this is the blast wave, then, G310.6–1.6 is a member of a very exclusive club of seven or eight Galactic shell SNRs whose X-ray spectra are dominated by synchrotron emission. (See Acero et al. (2016) for a current list of SNRs showing synchrotron emission.) However, in almost all those instances, and among the slightly larger collection of SNRs showing some evidence for a synchrotron component in a dominantly thermal spectrum, the shells show almost unresolved sharp edges over much of the periphery, certainly not the case for G310.6–1.6. The large ratio of PWN radius to shell radius here is highly unusual;

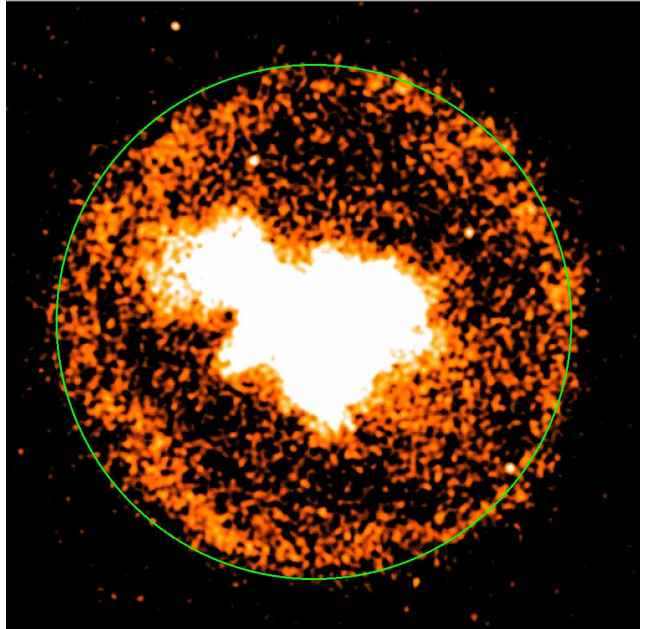


Figure 2. G310.6–1.6 with logarithmic scaling and smoothed with a $2''$ Gaussian. Note the extension of the PWN toward the shell in the NE, possibly reaching as far as the shell, and the clear evidence for a dust-scattering halo of emission from the PWN, inside the shell. The circle is centered on the pulsar with a radius of $75''$.

there appears to be little room for both shocked surrounding material and shocked ejecta. Finally, any interpretation of the shell as a blast wave requires a very peculiar supernova, as R10 noted. However, there is no obvious alternative interpretation of the shell. It is unlikely to be the PWN/ejecta interaction shock, as that shock is almost certainly too slow at any stage of SNR/PWN evolution to be able to accelerate particles to X-ray-emitting energies (velocities at least of order $800 - 1000 \text{ km s}^{-1}$ seem required). Additionally, that would require the existence of a large completely undetected surrounding shell SNR.

3. OBSERVATIONS

G310.6–1.6 was observed in November 2010 (M. Renaud, PI), and we observed it in three segments in November and December 2016 (see Table 1). The two epochs are separated by 6.035 yr. At each epoch, the remnant was placed on the Advanced CCD Imaging Spectrometer (ACIS) S3 array, and Very Faint mode was used in order to reduce the particle background. We used CIAO version 4.11 and CALDB version 4.8.4 to reprocess these observations. No significant particle flares were found. To retain the full (subpixel) *Chandra* spatial resolution, we used a standard processing option, the Energy-Dependent Subpixel Event Repositioning (EDSER) algorithm of Li et al. (2004), in reprocessed event files. We aligned all observations using the bright pulsar, and then merged the three 2016 segments together. The total effective exposure in 2016 is 142 ks, nearly 3 times as long as in 2010. No statistically significant displacement was found

Table 1. *Chandra* Imaging Observations of G310.6–1.6.

Date	Observation ID	Roll Angle (deg)	Effective Exposure (ks)
2010 Nov 17–18	12567	151	51
2016 Nov 25	17905	139	14
2016 Nov 29–30	19919	130	79
2016 Dec 5	19920	130	49

between the positions of background and foreground point sources at each epoch (after aligning observations using the pulsar). (There are only 10 rather faint sources with matching coordinates, so the alignment based on point sources is inferior to the alignment based on the pulsar alone.) We used CIAO tasks `dmcopy` and `specextract` to extract images and spectra from the reprocessed and aligned 2010 and 2016 event files at each epoch.

4. IMAGING

4.1. Shell

Figure 2 shows a smoothed image, highlighting the shell and faint emission between the PWN and the shell. The shell is remarkably circular; the circle in the figure is centered on the pulsar, with a radius of $75''$. While it is difficult to delineate the faint outer parts of the PWN, it appears that additional interior emission is present, expected due to dust scattering from the bright PWN given the high column density toward G310.6–1.6. B12 included such a component in their analysis of radially averaged profiles of the emission. Beyond the shell, this component forms a low-surface brightness X-ray halo surrounding the remnant.

A very rough estimate of the displacement of the pulsar from the center of a fit of the $75''$ -radius circle to the shell is about $6''$, or about $6 \times 10^{17} d_7$ cm. Even for a very young age of $700 d_7$ yr, the implied sky-plane speed is only about $280 d_7$ km s^{-1} .

There is a suggestion of emission all the way from the PWN to the shell in the NE. If material from the PWN is interacting with the outer shell, one might expect some spectral signature. We discuss this issue below.

4.2. PWN

The pulsar in G310.6–1.6 is bright, with an ACIS-S3 count rate of 0.075 ct s^{-1} within a circle of radius $4''$. The peak rate in the innermost 3×3 -pixel region is 0.053 ct s^{-1} , resulting in a modest amount of pileup, a reduction of order 8% of the total count rate. This is too low to result in significant image distortion due to pileup trails.

The pulsar-wind nebula has a very similar appearance in both the 2010 and 2016 epochs, with an irregular outline of mean radius about $30''$, but small structures near the pulsar have changed (Fig. 3). A bright spot near the pulsar (Knot

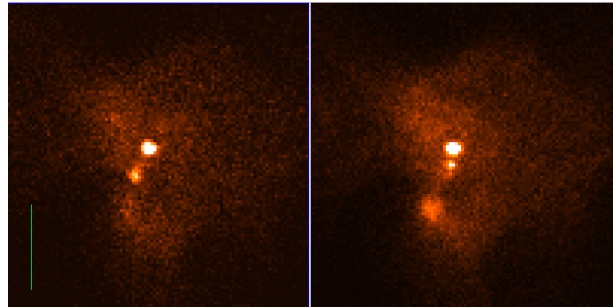


Figure 3. PWN in 2010 (left) and 2016 (right). The larger-scale structure has changed little, but features just to the south of the pulsar have changed markedly. No clear jet or torus-like feature is evident. The scale bar on the 2010 image has length $10''$.

1; see Fig. 4) has changed position by about $1.8''$ between 2010 and 2016, moving inward toward the pulsar. If this is a discrete object, as seems unlikely, the implied speed is about $10,000 d_7$ km s^{-1} , but a more likely explanation is a fading of the first knot and the appearance of a second one. In the 2016 image, the knot is separated from the pulsar by about $1.8''$, so the lower limit on the required proper motion from the pulsar is the same, about $10,000$ km s^{-1} , or about $0.03c$. For comparison, knots in the Vela pulsar-wind nebula are observed to move outward at $0.3 - 0.7c$ (Pavlov et al. 2003). However, spectral fits (see below) indicate that Knot 1 has not only faded, by about 20%, but has also changed spectral slope, increasing the likelihood that two distinct features are involved at the two epochs.

Knot 2, clearly visible in 2016, was only a faint enhancement of diffuse emission in 2010. Unlike Knot 1, it has not moved, but has brightened by 46% (see below) while maintaining the same photon index.

Roughly linear structures can be made out in the PWN at low flux levels (see Fig. 4), oriented approximately radially. However, these do not point exactly back to the pulsar position, so they are not pileup-trail artifacts.

5. SHELL MOTION AND AGE OF G310.6–1.6

No shell motion was detected between 2010 and 2016, ruling out a very young (< 1000 yr) age for G310.6–1.6. The short (6.0 yr) time baseline in combination with the lack of a sharp outer boundary and the faintness of the shell prevent us from establishing stringent constraints on the remnant's age. We briefly describe here our method used to measure expansion of the shell, and summarize the results obtained.

We extracted broadband (1–8.5 keV) images at each epoch, $182'' \times 182''$ in size, with an image pixel of $0.356'' \times 0.356''$, and encompassing the entire remnant. We used these images to measure the expansion of the shell with the help of a Bayesian method we employed previously in our study of the expansion of fast supernova ejecta in the very young remnant G330.2+1.0 (Borkowski et al. 2018). Our chosen image pixel is about half of the ACIS pixel in its surface area. This is still not enough to fully sample *Chandra*'s PSF near the optical axis and take full advantage of the EDSEER algorithm,

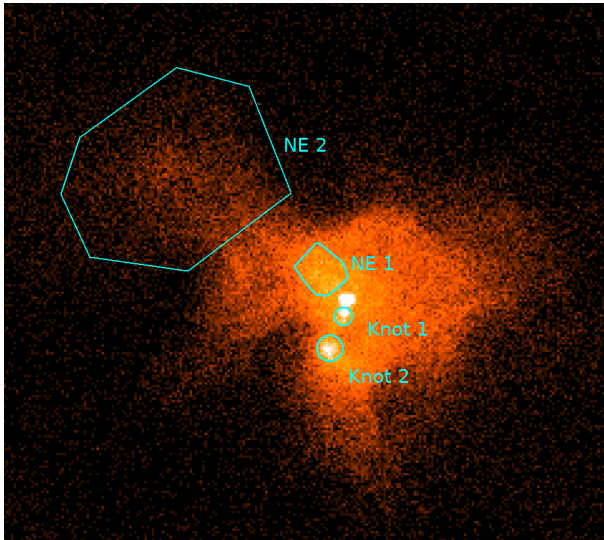


Figure 4. Regions described in the text, superposed on the 2016 image. The pulsar is immediately north of Knot 1. Square-root scaling was used.

but the mean number of counts per image pixel in the shell drops even further when images with still smaller pixel sizes are extracted from the event files. There is no advantage in using such extremely photon-starved images with our expansion measurement method.

The 2016 image was smoothed with the iterative variance-stabilization method of [Azzari & Foi \(2016\)](#). The smoothed image is shown in Figure 5, with the shell region where we measured expansion overlaid. The 2010 image did not require smoothing. We subtracted background from the smoothed 2016 image, and then corrected the background-subtracted image with a monochromatic ($E = 2.7$ keV) exposure map prior to expansion measurements. The background was modeled as a sum of a uniform background and an X-ray halo visible beyond the remnant’s outer boundary. This halo likely arises from scattering of X-rays produced by the pulsar and the PWN by dust along the line of sight to G310.6–1.6. The background-subtracted and exposure-corrected image was then allowed to shrink or expand (and also vary in surface brightness) during Markov chain Monte Carlo (MCMC) simulations using the PyMC software package ([Patil et al. 2010](#)). The background in 2010 was also modeled as a sum of a uniform background and the dust-scattering halo model just described. Poisson statistics was assumed for the unsmoothed 2010 image.

Expansion might not be centered exactly at the geometrical shell center even when an SNR shell appears nearly spherically symmetric (e.g., [Williams et al. 2013](#)). In order to allow for this possibility, we allowed the expansion center to vary in our MCMC simulations. A 2-D Gaussian prior for the expansion center was assumed, centered at the geometrical shell center, with a FWHM of $16.5''$ (i.e., $1\sigma = 7''$, one tenth of the remnant’s radius). With this width, the allowable displacement of the expansion center exceeds the pulsar’s dis-

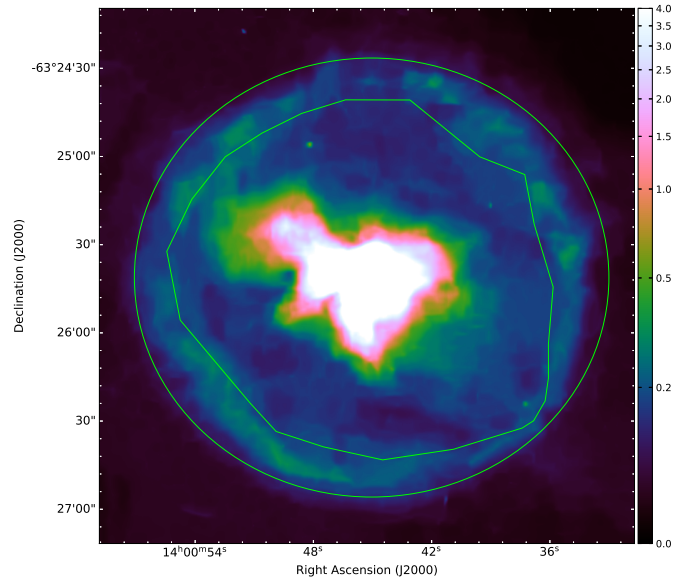


Figure 5. Smoothed *Chandra* image of G310.6–1.6 (1–8.5 keV), with the region shown where expansion of the shell was measured. The pulsar and the inner part of the PWN are saturated. Scale is in counts per $0.356'' \times 0.356''$ image pixel.

placement from the geometrical shell center. Uniform priors were used for the expansion and the surface brightness scaling factor.

MCMC simulations involved running 10 chains with 6000 samples each, with each thinned by a factor of 5. Only the results for the expansion rate are of interest here. (The surface brightness scaling factor does not differ significantly from unity once *Chandra*’s systematic flux calibration errors are taken into account, while the expansion center location cannot be meaningfully constrained in the absence of discernible shell motion.) The mean expansion rate is negative, $-0.04\% \text{ yr}^{-1}$, with the minus sign denoting contraction instead of expansion. However, the 90% credible interval of $(-0.14, 0.04)\% \text{ yr}^{-1}$ is consistent with no shell motion firmly detected. The posterior marginal probability distribution for the expansion rate is asymmetric, skewed towards negative values away from its maximum near $-0.025\% \text{ yr}^{-1}$.

Only the statistical errors arising from the counting noise in the 2010 image were taken into account in our MCMC simulations, so the errors quoted above underestimate the true errors. The counting noise in the 2016 image is relatively modest in comparison, leading to an increase in errors by about 16%, but other sources of error (e.g., such as arising from smoothing) have not been taken into account. So the true 90% credible interval for the expansion rate must be somewhat wider than obtained from our MCMC simulations. Nevertheless, fast expansion rates $\geq 0.1\% \text{ yr}^{-1}$ (corresponding to free expansion ages ≤ 1000 yr) are strongly disfavored. Instead, our expansion measurements indicate that G310.6–1.6 is most likely at least several thousand years old.

6. SPECTROSCOPY

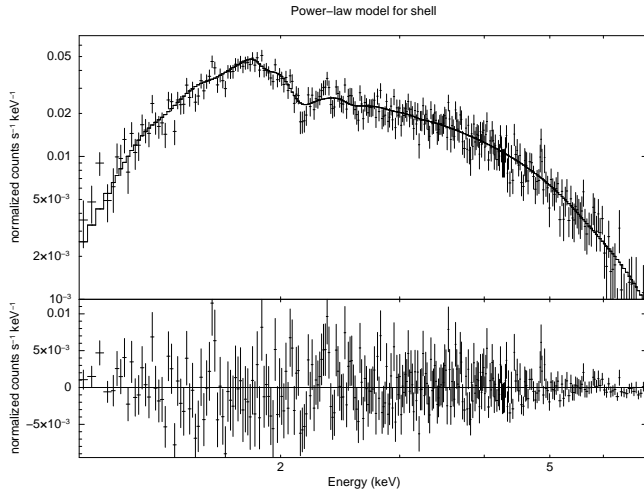


Figure 6. Shell spectrum, fit with power-law model. See text for details.

We analyzed our combined 142 ks total 2016 observation using XSPEC version 12.10 (Arnaud 1996), with Grevesse & Sauval (1998) abundances and Cash (1979) statistics. (Derived values for column densities can be significantly different when different abundance sets are used.) Unless otherwise noted, all fits were performed in the energy range of 0.8 to 7 keV, and all uncertainties are 90% confidence intervals. The background was modeled, not subtracted while fitting spectra, but only background-subtracted spectra are shown in Figures 6, 8, and 9. The particle background was modeled with a combination of Gaussians and power-laws, exponentially cut off at both low and high energies. Sky background near G310.6–1.6 includes the dust-scattering halo, which we modeled with an absorbed power law.

6.1. Spatially-integrated Shell Spectrum

We confirm with much better statistics the absence of spectral lines reported by R10 and B12, supporting synchrotron emission as the most likely emission mechanism. See Figure 6. The fit shown there reports a column density $N_{\text{H}} = 2.75(2.63, 2.88) \times 10^{22} \text{ cm}^{-2}$ and photon index $\Gamma = 2.55(2.47, 2.64)$. The (absorbed) flux between 0.8 and 7 keV is $1.1 \times 10^{-12} \text{ erg cm}^{-2} \text{ s}^{-1}$; for this column density, the unabsorbed flux is $2.59 \times 10^{-12} \text{ erg cm}^{-2} \text{ s}^{-1}$, for an X-ray luminosity of $1.5 \times 10^{34} d_7^2 \text{ erg s}^{-1}$.

We also fit the data with a simple `srcut` model (synchrotron radiation from a power-law distribution of electron energies with an exponential cutoff at some E_{max}). Apparently a radio counterpart to the X-ray shell has been detected (W. Robbins 2014, unpublished PhD dissertation)¹ but no details are available. Therefore, to constrain the fit, we use the upper limit to 1 GHz radio emission from the shell from R10: a surface brightness at 1 GHz of $2.3 \times 10^{-21} \text{ W m}^{-2} \text{ Hz}^{-1} \text{ sr}^{-1}$. We estimate a solid angle subtended by the shell of an

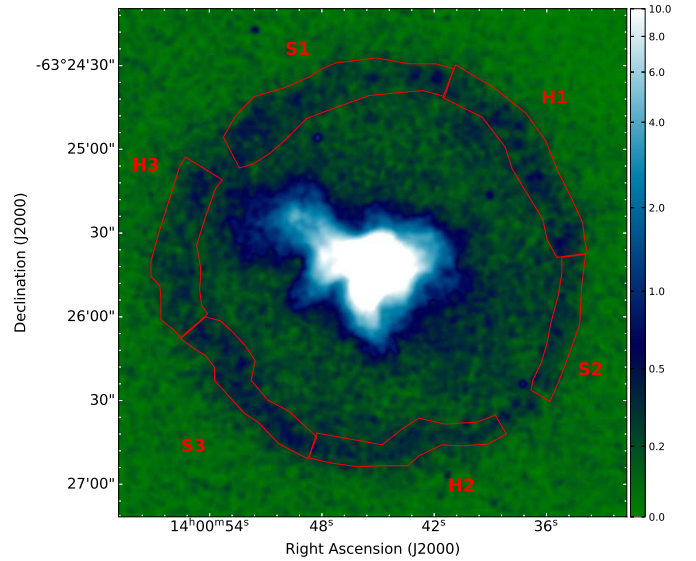


Figure 7. *Chandra* image of G310.6–1.6 (1–8.5 keV; based on combined 2010 + 2016 observations), smoothed with a Gaussian with the FWHM of $2''$, and overlaid with shell regions chosen for spectral analysis. Scale is in counts per $0.356'' \times 0.356''$ image pixel.

annulus of inner and outer radii of $50''$ and $70''$ respectively, or 2.1 arcmin^2 , and obtain an upper limit for the 1 GHz flux density of 40 mJy. With this value fixed, we obtain an energy spectral index of 0.49 (0.47, 0.50) applying to the power-law portion of the spectrum, and a rolloff frequency of 1.4 (1.1, 1.8) $\times 10^{17} \text{ Hz}$, quite reasonable values, and consistent with those found with the smaller datasets in R10 and B12.

To constrain the possible presence of thermal emission, we performed a two-component fit of a power-law plus plane shock (XSPEC model `pshock`). Lines are suppressed by a very low ionization timescale $\tau \equiv n_e t$: $3.1(0, 20) \times 10^8 \text{ cm}^{-3} \text{ s}$, where the 90% confidence interval includes zero. Thus the model fit is essentially a bremsstrahlung continuum, with temperature $kT_e = 2.2(1.4, 3.7) \text{ keV}$. The fitted emission measure corresponds to a pure-H rms density $n_e = 0.050(0.028, 0.070) d_7^{-1/2} \text{ cm}^{-3}$ assuming a volume filling factor of 0.25. It is clear that the shell is very faint, and the density very low; the preshock density n_0 is lower by a factor of the compression ratio which we take to be 4: $n_0 = 0.013(0.007, 0.018) d_7^{-1/2} \text{ cm}^{-3}$. In our fit, the thermal component is assigned about 27% of the total shell counts. However, the two-component model is not statistically preferable to our pure power-law model, so we conservatively treat the derived density as an upper limit.

6.2. Spectral Variations within the Shell

We chose 6 shell regions for detailed spectral studies (see Figure 7). They almost completely cover the entire shell, with only 2 narrow gaps excluded in order to avoid areas most strongly affected by out-of-time events originating in the pulsar/PWN system. The spectral hardness ratio

¹ Abstract available at <https://ses.library.usyd.edu.au/handle/2123/12378>

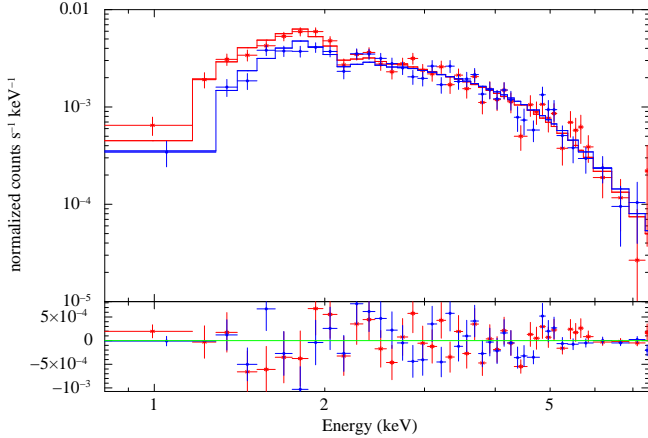


Figure 8. Shell spectra of Regions S1 (red stars) and H1 (blue circles). Best-fit models (solid lines) from Table 2 and residuals (data – model) are also shown.

$R = (H - S)/(H + S)$ (where S (H) is the number of detected source counts in the 1–2.5 (2.5–8.5) keV range) for these regions varies cyclically along the shell: $-7.5\% \pm 2.5\%$ and $8.8\% \pm 2.7\%$ for regions S1 and H1, $-7.1\% \pm 4.5\%$ ($0.3\% \pm 3.4\%$) for regions S2 (H2), and $-7.9\% \pm 2.9\%$ ($4.8\% \pm 3.1\%$) for regions S3 (H3) (errors here are 1σ). It is nearly the same among Regions S1, S2, and S3, implying little (if any) spectral variations between them. Fits with an absorbed power law confirm this lack of spectral variations, so we refer to the set of Regions S1, S2, and S3 as the soft region set S hereafter. Regions H1, H2, and H3 have significantly harder spectra than the soft region set S.

Fits with an absorbed power law give $N_{\text{H}} = 2.54(2.33, 2.76) \times 10^{22} \text{ cm}^{-2}$ and $\Gamma = 2.65(2.50, 2.82)$ for the region set S, and $N_{\text{H}} = 3.65(3.22, 4.12) \times 10^{22} \text{ cm}^{-2}$ and $\Gamma = 2.90(2.63, 3.18)$ for the hardest Region H1. Since the confidence intervals for N_{H} are well separated, we conclude that absorption varies significantly across the remnant. A joint fit to the region set S and Region H1, assuming the same intrinsic shell spectrum there but different N_{H} , gives $N_{\text{H}} = 2.62(2.43, 2.82) \times 10^{22} \text{ cm}^{-2}$ for the region set S, and $N_{\text{H}} = 3.39(3.13, 3.67) \times 10^{22} \text{ cm}^{-2}$ for Region H1, with $\Gamma = 2.72(2.58, 2.86)$. The hydrogen column N_{H} in Region H1 is 30% larger than within the region set S. This much larger than average N_{H} in Region H1 explains why the X-ray spectrum there is harder than elsewhere. Figure 8 graphically shows spectral differences between Regions S1 and H1.

We also fit spectra extracted from Regions H2 and H3 with an absorbed power law. Table 2 lists results of these fits as well as the results of the joint spectral fit just described, while Figure 9 shows how spectra and spectral fits differ between Regions S3 and H3. In Region H3, the maximum-likelihood value of $2.98 \times 10^{22} \text{ cm}^{-2}$ for N_{H} is intermediate between the region set S and Region H1, while $\Gamma = 2.56$ is slightly less than in these regions. So both high absorption and an intrinsically hard spectrum might be responsible for the harder than average spectrum of Region H3. But

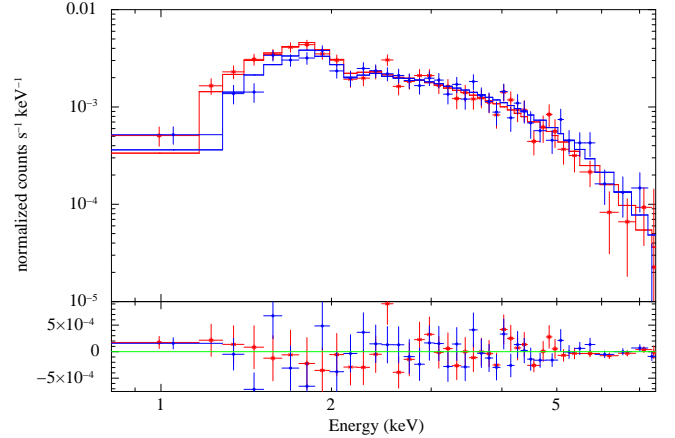


Figure 9. Shell spectra, best-fit models, and residuals for Regions S3 (in red) and H3 (in blue).

the errors on N_{H} and Γ are large enough to make it difficult to distinguish between high absorption and an intrinsically hard spectrum as the origin for the harder than average spectrum there. The hardness ratio in Region H3 is only marginally smaller than in Region H1. A joint fit to their spectra gives $N_{\text{H}} = 3.35(3.04, 3.68) \times 10^{22} \text{ cm}^{-2}$ and $\Gamma = 2.77(2.55, 2.96)$. This best-fit model is remarkably similar to the best-fit model for Region H1 listed in Table 2, confirming the spectral similarity of Regions H1 and H3. Just as for Region H1, high absorption alone can account for the hardness of Region H3. But in view of large errors for N_{H} and Γ (see Table 2), a hard intrinsic spectrum without any extra absorption remains a plausible alternative explanation.

Perhaps the most promising hint in favor of intrinsic spectral variations within the shell comes from Region H2, since the maximum-likelihood value of 2.4 for Γ is the lowest among all regions (Table 2). But N_{H} of $2.4 \times 10^{22} \text{ cm}^{-2}$ is also low, and since errors on N_{H} and Γ are large and they correlate very strongly in our fits, a higher than average absorption without any intrinsic spectral variations can also account for the difference in the spectral hardness of Region H2 and the region set S. By jointly fitting X-ray spectra from these regions, an increase in N_{H} that is enough to explain this difference is estimated to be at around 10%.

We conclude that substantial ($\sim 30\%$) spatial variations in the interstellar medium (ISM) column density N_{H} are present along the line of sight to G310.6–1.6, with the largest absorption detected in the northwest. Patchy absorption with relative variations of N_{H} up to several tens of percent can explain all spectral variations detected in its limb-brightened X-ray shell. Such structures can be seen in the direction of G310.6–1.6 in the DECAM Plane Survey (Schlafly et al. 2018). But this does not exclude a possibility that intrinsic spectral variations are as important as variations in the ISM absorption. In particular, origins of much harder than average spectra seen in the eastern shell are unclear at this time. This harder spectrum might be intrinsic to the remnant, perhaps related to the distorted eastern shell morphology. Alterna-

Table 2. Spatially-Resolved Shell Models

Region	N_{H} (10^{22} cm^{-2})	Γ	K^{a} ($10^{-4} \text{ ph keV}^{-1} \text{ cm}^{-2} \text{ s}^{-1}$)
S1	2.62(2.43, 2.82) ^b	2.72(2.58, 2.86) ^c	1.82(1.51, 2.22)
S2	2.62(2.43, 2.82) ^b	2.72(2.58, 2.86) ^c	0.58(0.48, 0.72)
S3	2.62(2.43, 2.82) ^b	2.72(2.58, 2.86) ^c	1.34(1.11, 1.63)
H1	3.39(3.13, 3.67)	2.72(2.58, 2.86) ^c	1.96(1.61, 2.42)
H2	2.43(2.04, 2.87)	2.37(2.08, 2.68)	0.69(0.46, 1.04)
H3	2.98(2.55, 3.45)	2.56(2.27, 2.86)	1.21(0.81, 1.86)

NOTE—Errors are 90% confidence intervals.

^aNormalization of power law at 1 keV.

^bAssumed the same in Regions S1 – S3.

^cAssumed the same in Regions S1 – S3 and H1.

tively, the ISM absorption might be nearly as high there as in the northwest.

6.3. Pulsar-Wind Nebula

For the spectrum of the PWN, we also find results consistent with previous work: $N_{\text{H}} = 2.89(2.85, 2.93) \times 10^{22} \text{ cm}^{-2}$ and $\Gamma = 2.07(2.05, 2.10)$. This value for the photon index is quite typical for PWNe (e.g., Kargaltsev et al. 2013). The absorption is marginally higher than that found for the S regions of the shell, and lower than that in H1 and H3, that is, within the range of variation we find in the shell. The unabsorbed flux of the PWN is $2.20(2.17, 2.24) \times 10^{-11} \text{ erg cm}^{-2} \text{ s}^{-1}$, or $1.3 \times 10^{35} \text{ erg s}^{-1}$ at a distance of 7 kpc. This is about 4×10^{-3} of the pulsar spindown power, also a typical fraction.

B12 reported that the spectrum of the PWN softens with distance from the pulsar, as observed in virtually all PWNe. At epoch 2016, the spectrum of Knot 1 near the pulsar at epoch 2016 is well-described by a featureless power-law with photon index $\Gamma = 1.67(1.49, 1.85)$, while Knot 2 has $\Gamma = 1.98(1.84, 2.13)$. A more diffuse region in the NE (NE 1 in Fig. 4) has $\Gamma = 1.87(1.78, 1.95)$, while fainter emission between the bright PWN and the shell, Region NE 2, shows a considerably steeper spectrum, $\Gamma = 2.39(2.30, 2.49)$, intermediate between the value in NE 1 and that in the shell. The difference between NE2 and the shell is marginally significant; if all regions are required to have the same column density as that from the fit to the full PWN, we find $\Gamma(\text{shell}) = 2.64 \pm 0.04$ and $\Gamma(\text{NE2}) = 2.30(2.26, 2.36)$ – significantly different. However, as we find substantial variations in N_{H} toward different regions of the shell, which we argue are significant, similar differences toward different regions of the PWN may also exist. We can say with confidence that the photon index of NE2 lies between that of the PWN as a whole and that of the shell.

Table 3. Fluxes of PWN knots

Epoch	Knot 1	Knot 2
2010	6.66 (5.81, 7.83)	5.40 (4.69, 6.39)
2016	4.76 (4.35, 5.27)	8.33 (7.68, 9.09)

NOTE—Fluxes are unabsorbed, in units of $10^{-13} \text{ erg cm}^{-2} \text{ s}^{-1}$ between 0.8 and 7 keV. Errors are 90% confidence.

In the 2010 observations, both Knots 1 and 2 had substantially different fluxes (see Table 3). Knot 1’s photon index may have changed; the 2010 values are 1.91 (1.67, 2.17), marginally consistent; for Knot 2, the values are very similar: 1.97 (1.84, 2.10). It is likely that the feature we label Knot 1 is two features at the two epochs. These changes have similar magnitudes to those observed in some other PWNe, such as Vela (Hui et al. 2017).

7. RESULTS AND DISCUSSION

Here we enumerate our results:

1. We find no measurable expansion of the shell in G310.6–1.6 with a lower limit on the expansion age (90% confidence) of 2500 yr, independent of distance. For a distance of 7 kpc, this corresponds to a current shock velocity of no more than 1000 km s^{-1} . If deceleration has occurred, the true age will be less than the expansion age.
2. We confirm the weakness of any thermal emission in the shell, with considerably better statistics than in prior observations. A two-component fit including a plane-shock component requires a very low density,

both because the emission is faint and because a very small ionization timescale is demanded by the absence of obvious spectral lines. We conservatively treat the thermal component as an upper limit.

3. Our power-law fits to the integrated shell spectrum are consistent with those of previous studies, confirming that synchrotron radiation is the dominant emission process.
4. We find spectral variations around the shell, most likely due to variations in the absorbing column, though changes in the intrinsic power-law slope cannot be ruled out.
5. Faint emission from the complex PWN extends in the NE perhaps as far as the shell. The shell structure in the NE shows suggestions of interaction with the PWN.
6. We detect dust-scattered halo emission from the PWN both interior and exterior to the shell.

We can use these results to constrain the remnant parameters, given different assumptions about the dynamics. The plane-shock spectral component of the shell emission gives a preshock density $n_0 \sim 0.013 (0.007, 0.018) d_7^{-1/2} \text{ cm}^{-3}$, and swept-up mass $M_{\text{sw}} \sim 0.031 (0.017, 0.043) d_7^{5/2} M_\odot$ if that density were uniform inside the present radius of G310.6–1.6. An age estimate of $t = \tau/n_e$ gives $200 d_7^{1/2}$ yr for the best-fit values of τ and n_e ; the 90% limit for both τ and n_e gives $2 \times 10^9 / 0.020$ s or about $2300 d_7^{1/2}$ yr, marginally consistent with the lower limit we find for the expansion age.

One fundamental question concerning this system is the nature of the shell itself. With no measurable expansion velocity, it poses major problems of interpretation.

7.1. Blast wave?

We can attempt to construct a Sedov blast wave given these observed quantities. The true age is less than the free-expansion age by 0.4, or at least 1000 yr; then the observed size gives a relation between explosion energy and preshock density of $E_{51} \lesssim 0.035 n_0 d_7^5$. In a Sedov blast wave, the emission-measure weighted ionization timescale $\langle \tau \rangle$ is about 0.2 times the remnant age times the immediate post-shock electron density (Borkowski et al. 2001), which can be compared with the mean ionization timescale in a plane-shock model, $\tau/2$. Our best-fit value of τ then implies a remnant age of $t \sim 2.5\tau/n_e \sim 500 d_7^{1/2}$ yr. Our 90% lower limit on density increases this to 900 years; pushing τ to its 90% upper limit allows us to reach the minimum age of 1000 yr. Then the swept-up mass is $0.017(n_0/0.017 \text{ cm}^{-3})M_\odot d_7^{5/2}$, giving an extremely low-energy explosion: $E \lesssim 3 \times 10^{47} d_7^{9/2}$ erg. The current shock speed can also be estimated from the fitted temperature $kT_e = 2.2 (1.4, 3.7)$ keV, giving $v_{sh} = 1400 (1100, 1800) \text{ km s}^{-1}$, assuming temperature equilibration between electrons and ions. In the absence of equilibration, the shock speed could be higher, but again, only the

90% lower limit assuming equilibration is consistent with the $\sim 1000 \text{ km s}^{-1}$ upper 90% limit we infer. This picture is roughly self-consistent; the current kinetic energy of expansion $M_{\text{sw}} v_s^2 / 2$ is $1.7 \times 10^{47} d_7^{9/2}$ erg, using the density derived from the plane-shock model emission measure, about twice the expected 0.3 times the explosion energy for a Sedov blast wave.

In order for this description to be even approximately self-consistent, the ejecta mass must be much smaller than the swept-up mass of $0.017 d_7^{5/2} M_\odot$. Our requirements on the explosion that could have produced G310.6–1.6 under this interpretation are extreme: an explosion energy 3000 times less than that for a typical core-collapse supernova, occurring in a region of far lower density than typical in the ISM. Even for the most extreme possible distance, $d_7 = 2$, the supernova energy is less than 6×10^{48} erg. A qualitatively similar but less quantitatively extreme conclusion was reached by R10 based on more general considerations. For an age of 1000 yr, the pulsar (at its current luminosity, since the spin-down age is much longer) has injected about 10^{48} erg, even more than the explosion energy. The supernova explosion energy is normally far larger than the pulsar-injected energy inferred for young PWNe; the fact that this is not the case here may be responsible for the unusually large PWN radius compared to the shell radius. If G310.6–1.6 is really in the Sedov phase, this also implies that the reverse shock has already returned to the center and recompressed the PWN, an event normally assumed to occur only after the pulsar luminosity has declined far below its birth value. However, the required characteristics of the explosion have no parallel in the study of SNRs.

7.2. Reverse shock?

By contrast, it is imaginable that the emission we see is dominantly from the inward-facing reverse shock, allowing an ejected mass comparable to rather than much smaller than the swept-up mass. The lack of observed expansion would imply that the self-similar ejecta-driven phase is ending and the reverse shock will be accelerating back toward the center of the remnant. (In fact, our nominal best value for the shell movement is a contraction at $0.04\% \text{ yr}^{-1}$, about 1000 km s^{-1} inward.) This explanation also comes at a high price: we must attribute the synchrotron emission to electrons accelerated at the reverse shock, a phenomenon not clearly observed in any other remnant. (However, very few remnants can be confidently assigned to the relatively brief evolutionary stage in which the reverse shock is moving back toward the remnant center with its peak strength.) The energetics arguments are still constraining: the observable kinetic energy is orders of magnitude less than the energy of typical supernovae. The absence of a clear torus-jet morphology as often seen in young PWNe might be taken as an argument against a scenario in which the reverse shock has not yet returned to crush the PWN, but the diversity of observed PWN morphologies and the clear unique features of G310.6–1.6 suggest that it would be premature to rule out any explanations on this basis.

7.3. Pulsar-fed emission?

An even more speculative solution attributes the shell emission not to any shock wave directly, but somehow to particles and magnetic field injected by the pulsar, perhaps through the PWN which appears to extend all the way to the inner edge of the shell in the northeast. There is no precedent for such an interpretation. High-resolution radio imaging would be very helpful here, in detecting or constraining morphological or spectral connections between the PWN and shell. Consistency, or contrast, of spectral-index or polarimetric properties, or particular morphological structures, could give clues to the relation.

7.4. Low-energy supernovae

All possibilities have in common the requirement of a very low-energy event (by supernova standards) giving rise to the observed pulsar and PWN. One avenue for a weak explosion leaving behind a neutron star is accretion-induced collapse (AIC) of a white dwarf in a binary. [Dessart et al. \(2006\)](#) describe the electron-capture core collapse and subsequent explosion (ECSN) of a massive white dwarf, ejecting a few $\times 10^{-3} M_{\odot}$ with a kinetic energy of $(2 - 3) \times 10^{49}$ erg, and leaving a neutron star. The obvious problem with such an origin for G310.6–1.6 is the lack of a binary system at present; unless the mass donor is completely accreted (“merger-induced collapse”), the supernova will not be adequate to unbind the system. Furthermore, the particular models of [Dessart et al. \(2006\)](#) result in highly asymmetric explosions, at odds with the very circular shell we observe. Finally, the rates of such unusual events are expected to be low ([Ruiter et al. 2019](#)). However, an anomalously faint supernova, SN 2008ha, has been interpreted as an ECSN, ejecting $0.1 - 0.3 M_{\odot}$ with a kinetic energy of $(1 - 5) \times 10^{49}$ erg ([Valenti et al. 2009](#)). Even these extreme examples of weak SNe fail to reach the requirements for G310.6–1.6.

The PWN would currently be in rough pressure balance with the interior of our extreme low-energy Sedov blast wave model. [R10](#) report a minimum equipartition energy of about $4 \times 10^{46} d_7^{17/7}$ erg, implying a pressure $E_{\min}/3V$ of about $10^{-10} d_7^{-4/7}$ dyn cm $^{-2}$. The Sedov central pressure $\sim 0.3\rho v^2$ is about $5 \times 10^{-11} d_7^{3/2}$ dyn cm $^{-2}$, using the lower limit to the thermal-gas density in the shell. Now E_{\min} is much less than the energy injected by the pulsar, so much of that energy has evidently been radiated.

Our upper limit for the current shock velocity of about $1000 d_7$ km s $^{-1}$ still allows for ongoing electron acceleration to X-ray emitting energies, where the rule of thumb requires a minimum shock speed of about 1000 km s $^{-1}$. In fact, the rolloff frequency of about 1.2×10^{17} Hz can easily be reached in 1000 years, for electron acceleration limited either by the remnant age or by synchrotron losses. According to expressions in [Reynolds \(2008\)](#): ignoring shock obliquity effects and defining $v_8 \equiv v(\text{shock})/10^8$ cm s $^{-1}$, we have

$$h\nu_{\text{roll}}(\text{age}) \sim 0.006 v_8^4 \left(\frac{t}{1000 \text{ yr}} \right)^2 \left(\frac{B}{10 \mu\text{G}} \right)^3 \text{ keV}$$

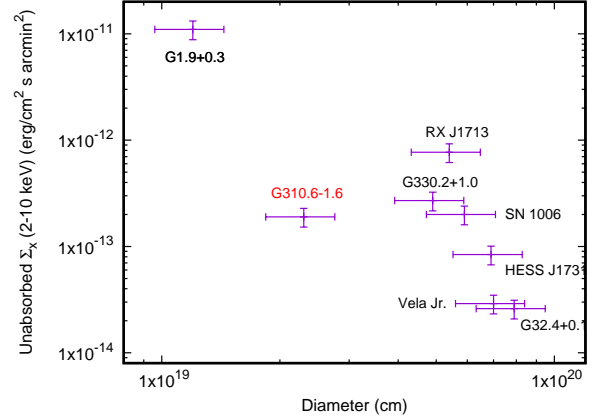


Figure 10. X-ray surface brightness-diameter plot for 8 Galactic synchrotron X-ray-dominated supernova remnants. Data: G1.9+0.3, RX J1713–3946, SN 1006, & Vela Jr., [Nakamura et al. \(2012\)](#); G330.2+1.0, [Torii et al. \(2006\)](#); HESS J1731–347, [Doroshenko et al. \(2017\)](#); & G32.4+0.1, [Yamazaki et al. \(2006\)](#). X-ray fluxes are between 2 and 10 keV, and generous uncertainties of 20% in both mean X-ray surface brightness Σ_x and D were assumed.

$$h\nu_{\text{roll}}(\text{loss}) \sim 0.3 v_8^2 \text{ keV.}$$

The operative value is the lower, so for the observed value of $h\nu_{\text{roll}} \sim 0.5$ keV, a magnetic field of $\sim 56 \mu\text{G}$ would allow acceleration to this value, with acceleration age-limited; if the actual shock velocity is lower than our upper limit of 1000 km s $^{-1}$, a higher field would be required, but this is conceivable, given some amplification as inferred for young SNRs (e.g., [Ressler et al. 2014](#)). But if B is much larger than this, losses would limit electron energy, requiring $v \sim 1300$ km s $^{-1}$, perhaps inconsistent with our limit, though more careful calculations would be required for these estimates to be certain.

This presumes the shell does represent the supernova blast wave. If the shell represents the reverse shock, the shock speed could be considerably higher, as undecelerated ejecta enter the roughly stationary shell and could do so at speeds at or above 1000 km s $^{-1}$, depending on the remnant age. But this explanation has other difficulties as mentioned above. If the shell is not a shock wave at all but some other kind of structure, even more problems arise, as particle acceleration to high energies is still required, but the true blast wave must be elsewhere and invisible. While the shell is faint, its mean surface brightness in X-rays is not too far below the trend seen in the distribution of X-ray synchrotron shells from Galactic remnants (see Fig. 10). Producing synchrotron emission in a slowly expanding ring that is not a shock wave would be challenging. Some mechanism for populating a shell with relativistic electrons from the PWN might be imagined, but such a hypothesis faces many difficulties.

The PWN in G310.6–1.6 is anomalously large as a fraction of the shell radius (if it is a blast wave), compared to other observed SNR/PWN systems. However, the estimates of van der Swaluw & Wu (2001) contain enough free parameters that the rough value of 0.4 we estimate for $R_{\text{PWN}}/R_{\text{SNR}}$ for G310.6–1.6 can still be accommodated, in the Sedov phase when the reverse shock has recompressed the PWN. If the shell is a reverse shock, those estimates do not apply, and the large size of the PWN relative to the shell is easily understandable. In this explanation, the reverse shock has yet to return and compress the PWN.

8. CONCLUSIONS

We have failed to find any measurable expansion of the highly circular shell of G310.6–1.6, placing a lower limit on the expansion age of about 2500 y, and an upper limit on the current shock velocity of about $1000(d/7 \text{ kpc}) \text{ km s}^{-1}$. The shell is very faint; its spectrum is featureless, almost certainly synchrotron emission. Upper limits to thermal emission allow us to deduce that if the shell locates the blast wave, a consistent description of G310.6–1.6 as a very young composite remnant in the Sedov phase is barely possible, with an age of 1000 yr. However, a very low-energy explosion is then required, with energy of less than about $3 \times 10^{47} d_7^{9/2}$ erg, and ejected mass much less than $0.02 d_7^{9/2} M_{\odot}$. The large size of the PWN relative to the shell could be a result of the very rapid deceleration of the blast wave; in 1000 yr, the pulsar

would deposit about 10^{48} erg in the PWN, an unusually high fraction (more than one!) of the explosion energy. While this interpretation has many problems, alternative explanations face substantial difficulties as well.

Progress on this fascinating object will require additional *Chandra* observations. A longer time baseline, and an exposure at least equal to the 142 ks we present here, should confirm expansion or contraction, or put strong limits on any changes, while improving the photon statistics for spectral analysis. The anomalies of G310.6–1.6 clearly require some unconventional explanations, which might advance our understanding of SNRs, PWNe, and their interaction.

We gratefully acknowledge support by NASA through *Chandra* General Observer Program grant SAO GO6-17062X. The scientific results reported here are based on observations made by the *Chandra* X-ray Observatory.

Software: CIAO (v 4.9) (Fruscione et al. 2006), ChIPS (Germain et al. 2006), XSPEC (Arnaud 1996), Astropy (Astropy Collaboration 2013), matplotlib (Hunter 2007), Numpy (van der Walt et al. 2011), PyMC (Patil et al. 2010), Scipy², APLpy (Robitaille & Bressert 2012)

Facilities: CXO

REFERENCES

- Acero, F., Ackermann, M., Ajello, M., Baldini, L., Ballet, J., et al. 2016, *ApJS*, 224, 8
- Arnaud, K. A. 1996, in *Astronomical Data Analysis and Systems V*, eds. G. Jacoby & J. Barnes, ASP Conf. Series, v.101, 17
- Astropy Collaboration, Robitaille, T. P., Tollerud, E. J., Greenfield, P., et al. 2013, *A&A*, 558, 33
- Azzari, L., & Foi, A. 2016, *IEEE Signal Processing Lett.*, 23, 1086
- Berthiere, C. 2012, bachelor's thesis, Laboratoire AstroParticules et Cosmologie, U. Tours (B12)
- Borkowski, K. J., Lyerly, W. J., & Reynolds, S. P. 2001, *ApJ*, 548, 820
- Borkowski, K. J., Reynolds, S. P., Williams, B. J., & Petre, R. 2018, *ApJL*, 868, L21
- Cash, W. 1979, *ApJ*, 228, 939
- Dessart, L., Burrows, A., Ott, C. D., Livne, E., Yoon, S.-Y., & Langer, N. 2006, *ApJ*, 644, 1063
- Doroshenko, V., Phlhofer, G., Bamba, A., Acero, F., Tian, W. W., Klochov, D., & Santangelo, A. 2017, *A&A*, 608, 23
- ² Jones, E., Oliphant, T., Peterson, P., et al. 2001, <http://www.scipy.org>.
- Fruscione, A., McDowell, J. C., Allen, G. E., Brickhouse, N. S., Burke, D. J., Davis, J. E., Durham, N., Elvis, M., Galle, E. C., Harris, D. E., Huenemoerder, D. P., Houck, J. C., Ishibashi, B., Karovska, M., Nicastro, F., Noble, M. S., Nowak, M. A., Primini, F. A., Siemiginowska, A., Smith, R. K., & Wise, M. 2006, *Proc. SPIE*, 6270, 62701V
- Germain, G., Milaszewski, R., McLaughlin, W., Miller, J., Evans, J. D., Evans, I., & Burke, D. 2006, *ASP Conf. Ser.*, 351, 57
- Grevesse, N., & Sauval, A. J. 1998, *Space Sci. Rev.*, 85, 1
- Hui, C. Y., Lee, J., Kong, A. K. H., Tam, P. H. T., Takata, J., Cheng, K. S., & Ryu, D. 2017, *ApJ*, 846, 116
- Hunter, J. D. 2007, *CSE*, 9.3, 90
- Kargaltsev, O., Rangelov, B., & Pavlov, G. G. 2013, [arXiv:1305.2552](https://arxiv.org/abs/1305.2552)
- Keek, S., Kuiper, L., & Hermsen, W. 2006, *ATel*, 810
- Li, J., Kastner, J. H., Prigozhin, G. Y., Schulz, N. S., Feigelson, E. D., & Getman, K. V. 2004, *ApJ*, 610, 1204
- Nakamura, R., Bamba, A., Dotani, T., Ishida, M., Yamazaki, R., & Kohri, K. 2012, *ApJ*, 746, 134
- Patil, A., Huard, D., & Fonnesback, C. J. 2010, *J. Stat. Software*, 35, 4
- Pavlov, G. G., Teter, M. A., Kargaltsev, O., & Sanwal, D. 2003, *ApJ*, 591, 1157

- Renaud, M., Marandon, V., Gotthelf, E. V., Rodriguez, J., Terrier, R., Mattana, F., Lebrun, F., Tomsick, J. A., & Manchester, R. N. 2010, *ApJ*, 716, 663 (R10)
- Ressler, S. M., Katsuda, S., Reynolds, S. P., Long, K. S., Petre, R., Williams, B. J., & Winkler, P. F. 2014, *ApJ*, 790, 85
- Reynolds, S. P. 2008, *ARA&A*, 46, 89
- Robitaille, T., & Bressert, E. 2012, *APLpy: Astronomical Plotting Library in Python*, Astrophysics Source Code Library, ascl:1208.017
- Ruiter, A. J., Ferrario, L., Belczynski, K., Seitenzahl, I. R., Crocker, R. M., & Karakas, A. I. 2019, *MNRAS*, 484, 698
- Schlafly, E. F., Green, G. M., Lang, D., Daylan, T., Finkbeiner, D. P., Lee, A., Meisner, A. M., Schlegel, D., & Valdes, F. 2018, *ApJS*, 234, 39
- Tomsick, J. A., Chaty, S., Rodriguez, J., Walter, R., & Kaaret, P. 2009, *ApJ*, 701, 811
- Torii, K., Uchida, H., Hasuike, K., Tsunemi, H., Yamaguchi, Y., & Shibata, S. 2006, *PASJ*, 58, L11
- Valenti, S., Pastorello, A., Cappellaro, E., Benetti, S., Mazzali, P. A., Manteca, J., Taubenberger, S., Elias-Rosa, N., Ferrando, R., Harutyunyan, A., Hentunen, V. P., Nissinen, M., Pian, E., Turatto, M., Zampieri, L., & Smartt, S. J. 2009, *Nature*, 459, 674
- van der Swaluw, E., & Wu, Y. 2001, *ApJL*, 555, L49
- van der Walt, S., Colbert, S. C., & Varoquaux, G. 2011, *CSE*, 13.2, 22
- Williams, B. J., Borkowski, K. J., Ghavamian, P., Hewitt, J. W., Mao, S. A., Petre, R., Reynolds, S. P., & Blondin, J. M. 2013, *ApJ*, 770, 129
- Yamazaki, R., Kohri, K., Bamba, A., Yoshida, T., Tsuribe, T., & Takahara, F. 2006, *MNRAS*, 371, 1975